Available online at www.sciencedirect.com
ScienceDirect
Acta Materialia 56 (2008) 6013–6026
Acta MATERIALIA
www.elsevier.com/locate/actamat

Quasicontinuum study of incipient plasticity under nanoscale contact in nanocrystalline aluminum

V. Dupont [a], F. Sansoz [a,b,*]

[a] School of Engineering, The University of Vermont, Burlington, VT 05405, USA
[b] Materials Science Program, The University of Vermont, Burlington, VT 05405, USA

Received 27 June 2008; received in revised form 7 August 2008; accepted 9 August 2008
Available online 13 September 2008

Abstract

Atomistic simulations using the quasicontinuum method are performed to examine the mechanical behavior and underlying mechanisms of surface plasticity in nanocrystalline aluminum with a grain diameter of 7 nm deformed under wedge-like cylindrical contact. Two embedded-atom method potentials for Al, which mostly differ in their prediction of the generalized stacking and planar fault energies, and grain boundary (GB) energies, are used and characterized. The simulations are conducted on a randomly oriented microstructure with $\langle 1\,1\,0\rangle$-tilt GBs. The contact pressure–displacement curves are found to display significant flow serration. We show that this effect is associated with highly localized shear deformation resulting from one of three possible mechanisms: (1) the emission of partial dislocations and twins emanating from the contact interface and GBs, along with their propagation and intersection through intragranular slip, (2) GB sliding and grain rotation and (3) stress-driven GB migration coupled to shear deformation. Marked differences in mechanical behavior are observed, however, as a function of the interatomic potential. We find that the propensity to localize the plastic deformation at GBs via interface sliding and coupled GB migration is greater in the Al material presenting the lowest predicted stacking fault energy and GB energy. This finding is qualitatively interpreted on the basis of impurity effects on plastic flow and GB-mediated deformation processes in Al.

Keywords: Nanoindentation; Molecular statics simulations; Aluminum; Nanocrystalline materials; Grain boundary migration

1. Introduction

Small-scale contact experiments, from simple microhardness testing to fully instrumented nanoindentation, have been used for some time to characterize the nature of yield phenomena and the influence of grain size on hardness and strengthening in nanocrystalline metals [1–7]. It is now well established in face-centered-cubic (fcc) metals and alloys that a marked transition in plasticity mechanism, accompanied by a continuous change in mechanical behavior, operates with a reduction of grain size from the microcrystalline to nanocrystalline regime [8–10]. Nanoscale contact probes are particularly well suited for the studies of plasticity transition in nanograined metals, because they can be highly sensitive to the heterogeneous nature of plastic deformation in very confined volumes of materials, and provide quantitative insights into the mechanisms governing incipient plasticity at reduced length scales.

In past work, nanoscale contact experiments in nanocrystalline metals have revealed two microstructure length scales producing different modes of plastic deformation. First, particular focus has been placed on examining how dislocations interact with surrounding grain boundaries (GBs) by performing nanoindentations at the center of single nanograins, that is, by forcing the contact area to be much smaller than the grain size. Yang and Vehoff [11] have observed that the dislocations, which nucleate below the indenter, only interact directly with the neighboring interfaces for grain sizes below 900 nm. At such scale, the

* Corresponding author. Address: School of Engineering, The University of Vermont, Burlington, VT 05405, USA. Tel.: +1 802 656 3837; fax: +1 802 656 1929.
E-mail address: frederic.sansoz@uvm.edu (F. Sansoz).

1359-6454/$34.00 © 2008 Acta Materialia Inc. Published by Elsevier Ltd. All rights reserved.
doi:10.1016/j.actamat.2008.08.014

point of elastic instability is clearly defined by a pop-in event whose width is strongly correlated to the size of the indented grain. The smaller the grain size, the smaller the pop-in width and the harder the material. For grain sizes comparable to the contact area, however, Minor et al. [12] have revealed using in situ transmission electron microscopy (TEM) nanoindentation that significant dislocation activity takes place in ultrafine-grained Al thin films before the first obvious jump in displacement in the load–depth nanoindentation curves. This result challenged the prevailing notion that the first pop-in event corresponding to the onset of plasticity during nanoindentation occurs in a dislocation-free crystal.

The second microstructure length scale at which past nanoscale experiments have been performed corresponds to contact areas much larger than the mean grain size. In this case, it is the collective deformation of the nanocrystalline GB network that dominates the plastic behavior. All experimental evidence shows that the pile-up of deformation left around residual impressions varies dramatically from homogeneous at large grain size (>20 nm) to inhomogeneous with intense plastic deformation in highly localized shear bands for very small grain sizes (<20 nm) [7,9,13,14]. Since shear band propagation is routinely observed in bulk amorphous metals under nanoindentation [15–20], it was suggested that the plastic deformation of nanocrystalline fcc metals with the finest grain size is comparable to the shear localization processes observed in bulk metallic glasses [21,22]. This assumption has recently been confirmed by the nanoindentation study of Trelewicz and Schuh [9] in nanocrystalline Ni–W alloys.

Contact plasticity at the former length scale has been well documented using atomistic modeling, because the underlying mechanisms are clearly defined by slip events and slip–GB interactions. A predictive understanding of the atomic mechanisms leading to shear localization under an indenter at very small grain sizes, however, has proved elusive, primarily for two reasons:

- It is commonly acknowledged that the GB networks play a critical role in the process of plasticity in nanocrystalline metals. But GBs can also be involved in simultaneous, yet different, plasticity mechanisms at very small grain sizes. These mechanisms include sources and sinks for lattice dislocations [23–25], GB sliding [14,26–28], grain rotation-induced shear band formation and grain coalescence [28–35], and GB migration coupled to shear deformation [35–41]. From past nanoindentation experiments, there is no clear consensus whether one or several of these atomic mechanisms truly dominate the onset of plasticity for the finest grain size. In particular, stress-assisted grain growth under an indenter has been observed at the onset of plasticity of nanograined Al and Cu with a mean grain size of 20 nm [42–44]. In a second group of nanoindentation experiments, however, neither grain growth nor GB migration processes have been observed in nano-Cu and NiAl with a mean grain size of 14 nm and 10 nm, respectively. Instead, it was concluded that the onset of plasticity was related to the nucleation of lattice dislocations from GBs [45,46]. Another study in plated Cu thin films with a 10 nm-grain size reported some evidence of void formation at GBs and triple junctions as a consequence of GB sliding during indentation [10].
- Earlier attempts made to model the nanoindentation of nanocrystalline metals by atomistic simulations have employed a spherical repulsive force to model virtual tips varying from 30 to 98 Å in diameter [47–54]. As such, contact areas were, to a large extent, smaller than the grain size, and the plastic zone produced by these tips was only limited to one or two grains. In contrast, some recent studies [22,55–58] have shown that it is critically important to simulate nanoindentation tips with more realistic sizes, in order to put into perspective the collective plastic processes of the GB networks in nanocrystalline materials. Using quasicontinuum simulations, we have previously reported the simulation of stress-assisted grain growth [55–57], and extended shear localization and banding by GB sliding and intragranular slip [22,57] in nanocrystalline Al deformed by a 300 Å diameter indenter, i.e. four times as large as the grain size studied. Similarly, Szulfarska et al. [58] have simulated the nanoindentation of normally brittle nanocrystalline ceramics with the same ratio between tip diameter and grain size, which revealed unusual GB-mediated plastic behavior. Furthermore, past simulations have used different embedded-atom-method (EAM) potentials, from which predictions of stacking fault energies can lead to strong differences within the same metal [59]. The impact of the interatomic potential on collective plastic processes, however, has never been fully characterized. The present atomistic study describes an effort to re-examine the relationship between interatomic potential and incipient plasticity mechanisms in a model nanocrystalline fcc metal film deformed by a wedge-like cylindrical tip, the size of which is notably larger than the mean grain diameter in the film.

This paper is divided as follows: Section 2 presents the details of the computational procedure used to simulate plane-strain contact in an Al thin film with a mean grain diameter of 7 nm using the quasicontinuum method. Two EAM potentials for Al are used and characterized in terms of generalized planar and stacking fault energies, as well as, GB energies for three types of $\langle 1\,1\,0\rangle$ symmetric tilt bicrystals. Their effects on the nanoindentation response and plastic behavior are presented in Section 3. A detailed analysis of incipient plasticity mechanisms mediated by GBs is also presented in this section. In Section 4, we show that incipient plasticity is strongly dependent upon the interatomic potential during the simulated indentation of nanocrystalline Al. An attempt is made to account for this

finding by taking into consideration the role of impurities in enhancing, rather than inhibiting, plasticity in fcc metals.

2. Computational methods

2.1. Quasicontinuum simulation

A multiscale computer model of a wedge-like cylindrical nanoindentation in a 200 nm thick nanocrystalline Al film was created using the quasicontinuum method [60]. This method predicts the equilibrium configuration of a system of atoms by energy minimization, given externally imposed forces or displacements; however, the atoms of the simulation are not all explicitly represented, as opposed to conventional molecular statics simulation. Such approach enables to model large-scale atomistic systems without the limitations of fixed or periodic boundary conditions encountered in classical molecular simulations. In this study, the region subjected to small deformation gradients outside the plastic zone was treated by finite elements with an atomistically informed elastic behavior [60], while the contact region at the interface between the indenter and film surface was fully represented by individual atoms. The film dimensions were 400 nm × 200 nm × 0.286 nm, and the size of the full atomistic zone was 50 nm × 25 nm × 0.286 nm, as indicated in Fig. 1a. Plane-strain contact was modeled by displacing a single crystal Al cylinder with a radius of 15 nm, along the direction normal to the top surface of the film. The indenter was oriented along the crystallographic directions shown in Fig. 1b and kept completely rigid during the simulation.

The polycrystalline structure of the film was constructed as follows. Reference atoms were placed randomly in the sample at an average distance equal to a pre-defined grain size. GBs were created by a Voronoi construction, which was based on a constrained-Delaunay connectivity scheme [61]. Starting from the reference atom, all atoms in the grains were added using the Bravais lattice vectors. For this study, the mean grain size was kept on the order of 7 nm. A total number of 50 grains were included in the full atomistic zone under the indenter. Each grain was assigned a common tilt axis along the [1–10] direction, and random in-plane orientation. To avoid discontinuities in the energy state during force minimization, the continuum/atomistic frontier was modeled as a single crystal interface whose crystallographic orientations are shown in Fig. 1a. We note that no significant atomistic activity was found near this interface, indicating that the plastic deformation was limited to the polycrystalline region during the simulations. The bottom of the film was fixed along each direction, while both sides of the model were left free. A spacing of 10 Å was initially imposed between the tip apex and the film surface. Periodic boundary conditions were imposed along the out-of-plane direction in the entire model. Therefore, this study focuses on a randomly oriented 2-D columnar microstructure. A caveat here is that the plastic deformation

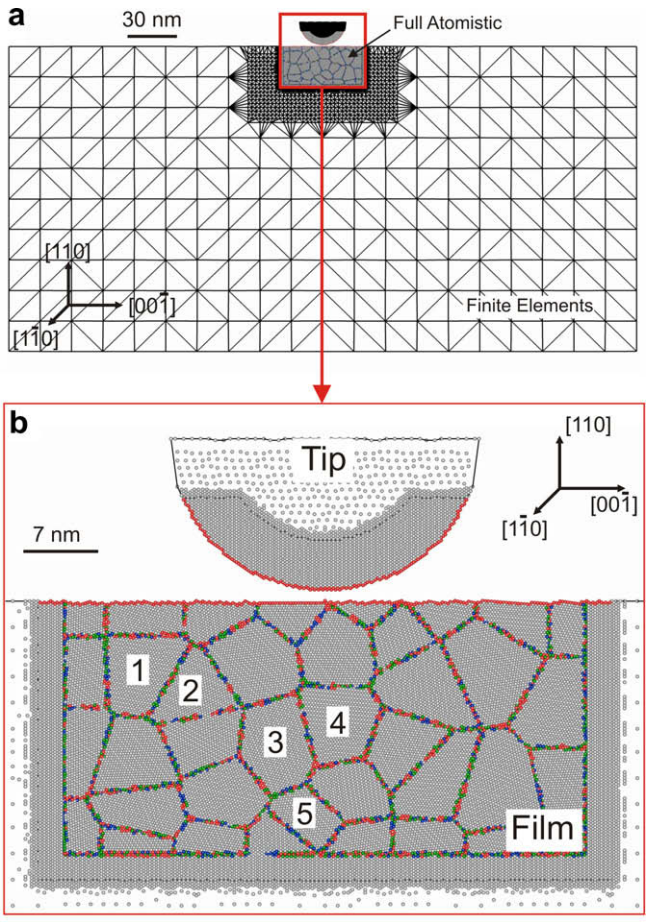

Fig. 1. Quasicontinuum computer model of a nanocrystalline Al thin film with a mean grain size of 7 nm deformed by a wedge-like cylindrical tip of 30 nm in diameter. (a) Full size view of both finite element and full atomistic domains. (b) Close-up of the full atomistic region near the contact zone after force relaxation.

processes in this type of microstructure may differ from those found in fully 3-D polycrystalline structures.

The total energy was minimized by conjugate gradient method until the addition of out-of-balance forces over the entire system was found less than 10^{-3} eV Å^{-1}. The sample was first relaxed under zero pressure condition in order to obtain the lowest state of energy. After relaxation, the atoms of the indenter were displaced by increments of 0.9 Å until a total displacement of 90 Å, corresponding to an indentation depth of 80 Å. Energy minimization was performed between each loading step. The centro-symmetry parameter [62] was calculated after each relaxation step to analyze the presence of planar defects in the lattice and the structure of the GB network during deformation. Our coloring scheme for this parameter was to color atoms in perfect fcc sequence in gray, those with hexagonal close-packed (hcp) structure or representing a stacking fault in blue, surface atoms in red and all other, non-coordinated atoms in green.

The semi-empirical EAM potentials for Al by Voter and Chen [63] and Mishin et al. [64] were used. For brevity in the following, these two potentials are referred to as

Al-VC and Al-MF potentials, respectively. For each potential, we adopted the quasicontinuum procedures used previously by Sansoz and Molinari [65,66] to calculate the generalized planar and stacking fault energy curves and the GB energy of three $\Sigma\langle 1\,1\,0\rangle$ tilt bicrystals, including $\Sigma 3(1\,1\,2)$, $\Sigma 9(2\,2\,1)$ and $\Sigma 11(1\,1\,3)$ symmetric tilt GBs.

2.2. Contact pressure calculation

The force applied by the indenter was calculated using the formula:

$$P = \sum_{i \in Z} P_i \tag{1}$$

where Z represents all atoms of the film belonging to the contact zone and P_i is the out-of-balance force on atom i in this zone, projected along the direction of indentation. The contact zone was computed after each loading step by only including atoms at the indenter–film interface within a separation distance from the tip equal to the potential cutoff radius. The cutoff radii were 5.555 and 6.287 Å for the Al-VC and Al-MF potentials, respectively. The mean contact pressure was determined at each step as:

$$H = \frac{P}{2a \times z_{\text{perio}}} \tag{2}$$

where a is the contact length, defined as half the width of the projected contact area, and z_{perio} is the thickness of our sample in the out-of-plane direction. The following criterion was used to quantitatively assess the onset of plasticity as obtained by the simulations. We computed the theoretical pressure–displacement curve corresponding to an isotropic elastic surface in contact with a rigid cylinder by using the following equation from continuum theory [67]:

$$\delta = F\frac{(1-\nu^2)}{\pi E}\left[2\ln(2t/a) - \nu/(1-\nu)\right] \tag{3}$$

where F is the total linear force in N m^{-1} ($=P/z_{\text{perio}}$), δ is the indentation depth, t is the film thickness along the direction of indentation, and E and ν are the Young's modulus and Poisson's ratio of the film, respectively. Substituting this into Eq. (2) gives the mean contact pressure for an elastic surface H^{e} such as:

$$H^{\text{e}} = \frac{\pi E}{2a(1-\nu^2)\left[2\ln\left(\frac{2t}{a}\right) - \frac{\nu}{1-\nu}\right]} \times \delta \tag{4}$$

Since the above equation depends on the contact length a, which changes with the penetration δ, the parameter H^{e} was re-evaluated at each loading step. Assuming $\nu = 0.345$ for polycrystalline Al [68], the isotropic Young's modulus was determined by fitting the elastic contact pressure H^{e} from Eq. (4) to the first portion of the curve obtained by quasicontinuum simulation (see Section 3.3).

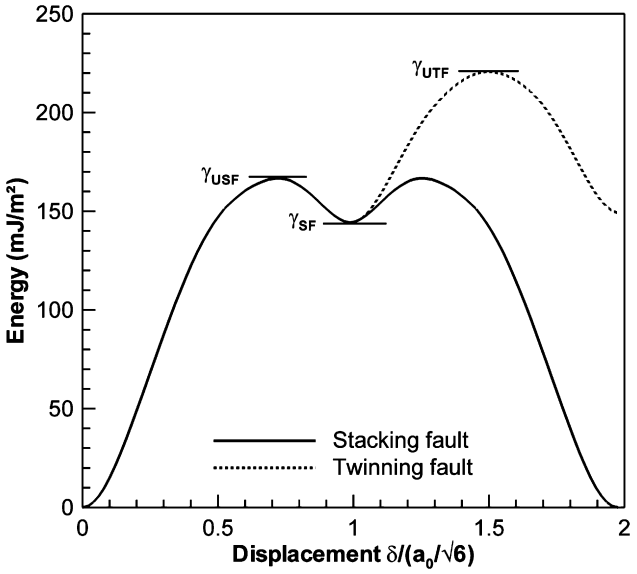

Fig. 2. Generalized stacking and planar fault energy curves obtained by quasicontinuum method with the Mishin–Farkas EAM potential for Al.

3. Results

3.1. Characterization of the EAM potentials

The generalized stacking and planar fault energy curves for the Al-MF potential are shown in Fig. 2. The unstable

Table 1
Stacking fault energy (γ_{SF}), unstable stacking fault energy (γ_{USF}), unstable twinning fault energy (γ_{UTF}) and GB energy (γ_{GB}) for three Σ tilt symmetric grain boundaries calculated from quasicontinuum method on the two EAM Al potentials investigated, and reference values from first-principles simulations for pure Al and Al with impurities

Energy	Present atomistic study		First-principles simulations	
	EAM Al-VC[a]	EAM Al-MF[b]	Pure Al	Al with impurities
γ_{USF}	93.04	166.71	175–224[c]	97[d]
γ_{SF}	75.41	144.22	120–166[c,e]	73[d], 82[f]
γ_{UTF}	120.99	220.72	207[g]	–
$\gamma_{\text{SF}}/\gamma_{\text{USF}}$	0.81	0.86	0.73–0.9	0.75
$\gamma_{\text{UTF}}/\gamma_{\text{USF}}$	1.30	1.32	0.92–1.18	–
$\gamma_{\text{GB}} - \Sigma 9(2\,2\,1)$	302	454	408[h]	–
$\gamma_{\text{GB}} - \Sigma 11(1\,1\,3)$	96	151	190–206[i,j]	96[j]
$\gamma_{\text{GB}} - \Sigma 3(1\,1\,2)$	318	355	426[i]	–

All units of energy are in mJ m^{-2}.
[a] Ref. [63].
[b] Ref. [64].
[c] Refs. [73–75].
[d] Al + 14.3 at.% solute H impurities [77].
[e] Refs. [70–72].
[f] Al + 3.3 at.% solute Ge impurities [78].
[g] Ref. [76].
[h] Ref. [79].
[i] Ref. [80].
[j] Al + 9 at.% substitution Ga impurities [81].

stacking fault energy (γ_{USF}), stacking fault energy (γ_{SF}) and unstable twinning fault energy (γ_{UTF}) are also indicated in this figure. As pointed out by Van Swygenhoven et al. [69], the ratios γ_{SF}/γ_{USF}, and $\gamma_{UTF}/\gamma_{USF}$ are most important in assessing the activation energy required to predict the nucleation of stacking faults, full dislocations or twins in the material. More specifically, if γ_{SF}/γ_{USF} is close to 1, the activation energy to create a trailing partial is low, which favors the nucleation of full dislocations. In contrast, if this ratio is closer to 0, the activation energy is too high, which decreases the propensity to nucleate trailing partials, leaving only stacking faults after propagation of the leading partial dislocations. The same reasoning can be made for twinning, which is more likely to occur if the ratio $\gamma_{UTF}/\gamma_{USF}$ is close to 1. The energy values obtained for both potentials are summarized in Table 1, along with reference values from first-principles simulations for pure Al [70–76] and Al with either H or Ge solute impurities [77,78]. In this table, we find that the calculated energy values are significantly smaller for the Al-VC potential than the Al-MF potential, which is consistent with the predicted values in the literature [64]. Similarly, the first-principle values for γ_{SF} and γ_{USF} are found to be lower when adding solute impurities to Al. Therefore, our finding is the predicted tendency that the stacking and planar fault energy values calculated from the Al-MF potential are consistent with the ab initio values for pure Al, while the Al-VC results seem to be in better agreement with the energy values for Al with impurities. In addition, we find that all the ratios γ_{SF}/γ_{USF} and $\gamma_{UTF}/\gamma_{USF}$ are similar and equal to 0.81–0.86 and 1.30–1.32, respectively, which suggests the same slip and twinning behavior regardless of the interatomic potential for Al.

3.2. Effects of EAM potential on GB structure and energy at equilibrium

Table 1 shows a significant increase in GB energy for the $\Sigma3(1\,1\,2)$, $\Sigma9(2\,2\,1)$ and $\Sigma11(1\,1\,3)$ symmetric tilt bicrystals, from the Al-VC potential to the Al-MF potential. This result is in good qualitative agreement with the difference in stacking fault energies found above for the two potentials. For comparison, Table 1 also shows the GB energy values obtained by first-principles for the same Σ tilt GBs in pure Al [79,81], as well as for a $\Sigma11(1\,1\,3)$ STGB containing substitution Ga impurities [81]. This comparison confirms the predicted trend found in Section 3.1, that the Al-VC potential better describes the GB energy of low Σ STGBs containing impurities than the Al-MF potential.

Furthermore, a statistical analysis of the misorientation angle and asymmetry of the GBs in our model is presented in Fig. 3. In this figure, the angles ψ and ψ' represent the angle between the [110] lattice direction and the GB plane for two neighboring grains, respectively. The sum $\psi + \psi'$

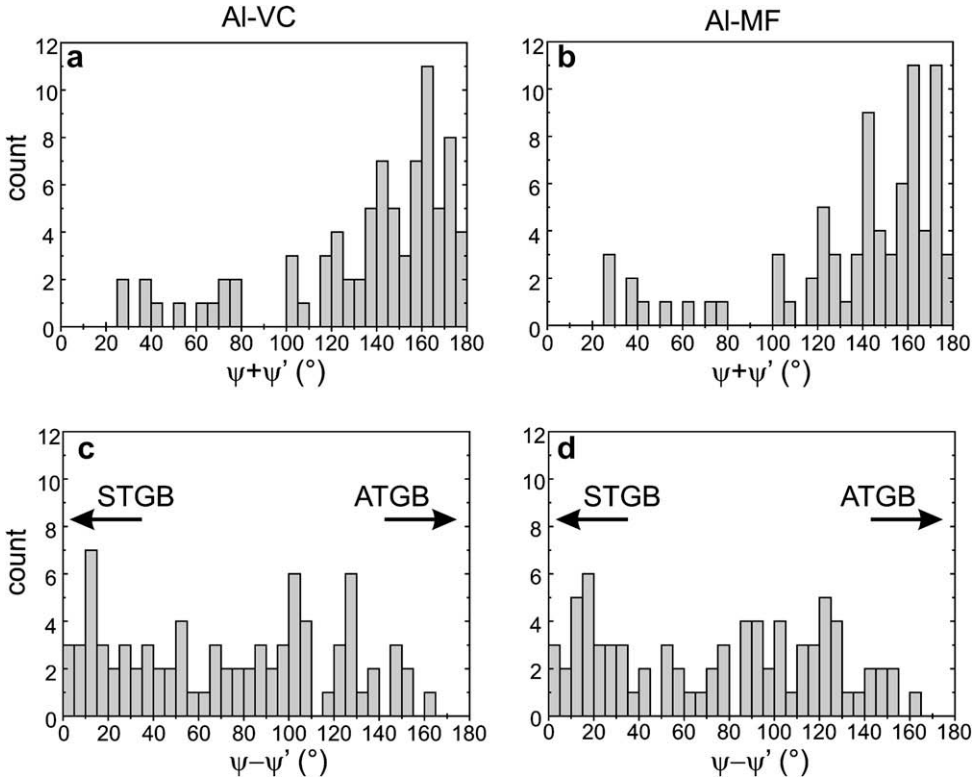

Fig. 3. Statistics of misorientation angle and GB structure in simulated nanocrystalline Al films after force relaxation as a function of interatomic potential. (a and b) Distribution of misorientation angles ($\psi + \psi'$) between grains. (c and d) Degree of symmetry of the GB structure from perfectly symmetrical tilt GB (STGB, $\psi - \psi' \sim 0$) to highly asymmetrical tilt GB (ATGB, $\psi - \psi' \sim 180°$).

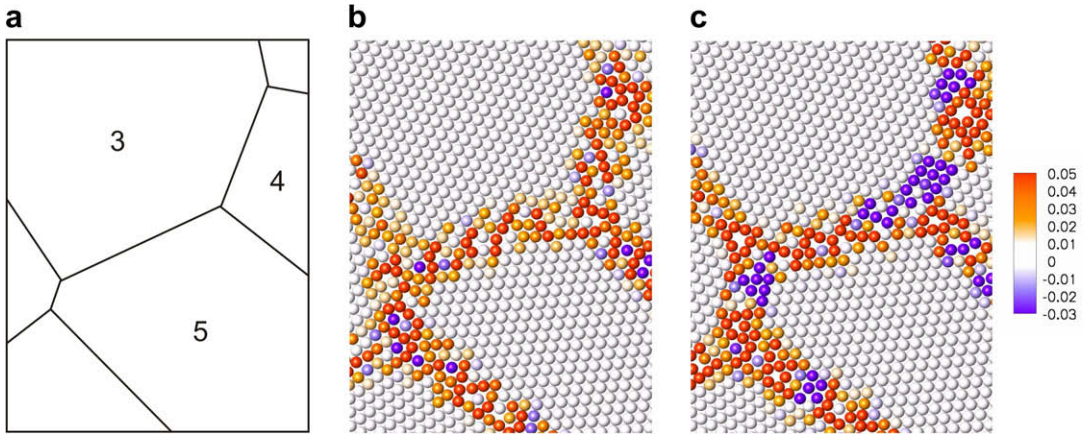

Fig. 4. Atomic energies (in eV) calculated after relaxation of a cluster of 6 nanograins in the contact zone. (a) Schematic representing the GB distribution and corresponding grain number as indicated in Fig. 1. (b) Voter–Chen EAM potential. (c) Mishin–Farkas EAM potential.

characterizes the misorientation angle at the boundary separating two grains. Low-angle GBs are represented by either $\psi + \psi' \leqslant 15°$ or $\psi + \psi' \geqslant 165°$, while high-angle GBs are defined by $15° < \psi + \psi' < 165°$. Some minor differences in the misorientation angle $\psi + \psi'$ are observed due to the rearrangement of microstructure after relaxation, even though the original model is identical. It can, however, be concluded from Fig. 3a and b that the distribution of misorientation angle and, therefore, the overall microstructure of the GB network are not significantly affected by the potential. In addition, the difference $\psi - \psi'$ represents the degree of symmetry of the GB, where $\psi - \psi' = 0°$ corresponds to perfectly symmetric tilt GBs (STGB), and $\psi - \psi' = 180°$ to highly asymmetric tilt GBs (ATGB). In Fig. 3c and d, the degree of symmetry appears to be homogeneous all along the set of values for $\psi - \psi'$. Also, there are only three perfectly symmetric GBs with $\psi - \psi' < 5°$, which is expected as the grains are ascribed random crystallographic orientation.

In addition, Fig. 4 shows a cluster of six nanograins present in the same nanostructure. This figure shows that the local atomic energy and structure at GBs are dramatically changed by the interatomic potential, despite the same misorientation angles between grains. In particular, we can observe that more GB atoms at the boundary between grains 3 and 5 present some highly negative values of energy in the Al-MF potential than the Al-VC potential. This observation could indicate that the bonding properties of the GBs are quite different between the two cases, as shown below.

3.3. Mechanical response under nanoscale contact

The evolution of the contact pressure as a function of the depth of indentation δ is represented in Fig. 5. Close-up views for $\delta < 20$ Å are shown in Figs. 6 and 7 for the Al-VC and Al-MF potentials, respectively. It is worth noting that there is a finite contact pressure at zero indentation depth, because adhesion forces between the tip and film

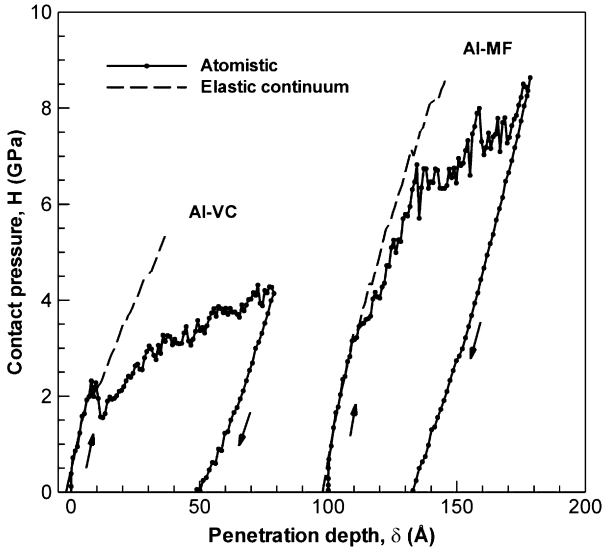

Fig. 5. Representative contact pressure–displacement curves from quasicontinuum simulation using Al-VC and Al-MF interatomic potentials. The curve for the Al-MF potential has been shifted to the right for clarity. The dashed curves correspond to the contact response of an isotropic elastic surface deformed by a rigid, wedge-like cylinder, as obtained from continuum theory.

surface exist in our model. As such, a shift to the left is required in the elastic continuum curves in order to obtain a good fitting between atomistic and elastic theory. The isotropic Young's moduli obtained from these fits are $E = 55$ GPa and $E = 66$ GPa for the Al-VC and Al-MF potentials, respectively. In comparison, the elastic moduli calculated by using the stiffness matrix constants of each potential are found equal to 57.6 and 70.8 GPa for the Al-VC and Al-MF potentials, respectively, which shows an excellent agreement between atomistic and theoretical values.

Both curves in Fig. 5 also show some significant flow serration at larger depth of indentation, which is indicative of localized shear deformation [21,22]. In this figure, the

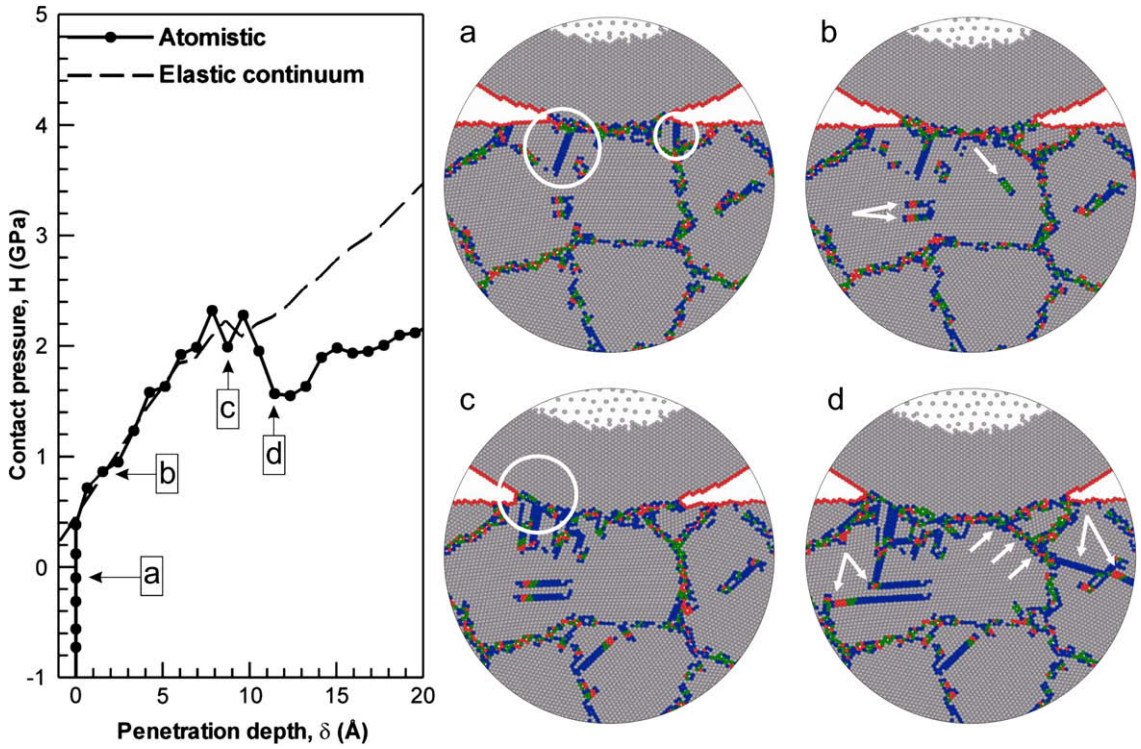

Fig. 6. Evolution of contact pressure as a function of penetration depth for shallow indentation using the Al-VC potential. Close-up views represent atomic details of deformation in the contact region. (a) Nucleation of the very first dislocation. (b) Nucleation and evolution of new dislocations. (c) Drop in curve corresponding to a sudden increase in contact area, just before yield point. (d) Nanocrystals after yield point.

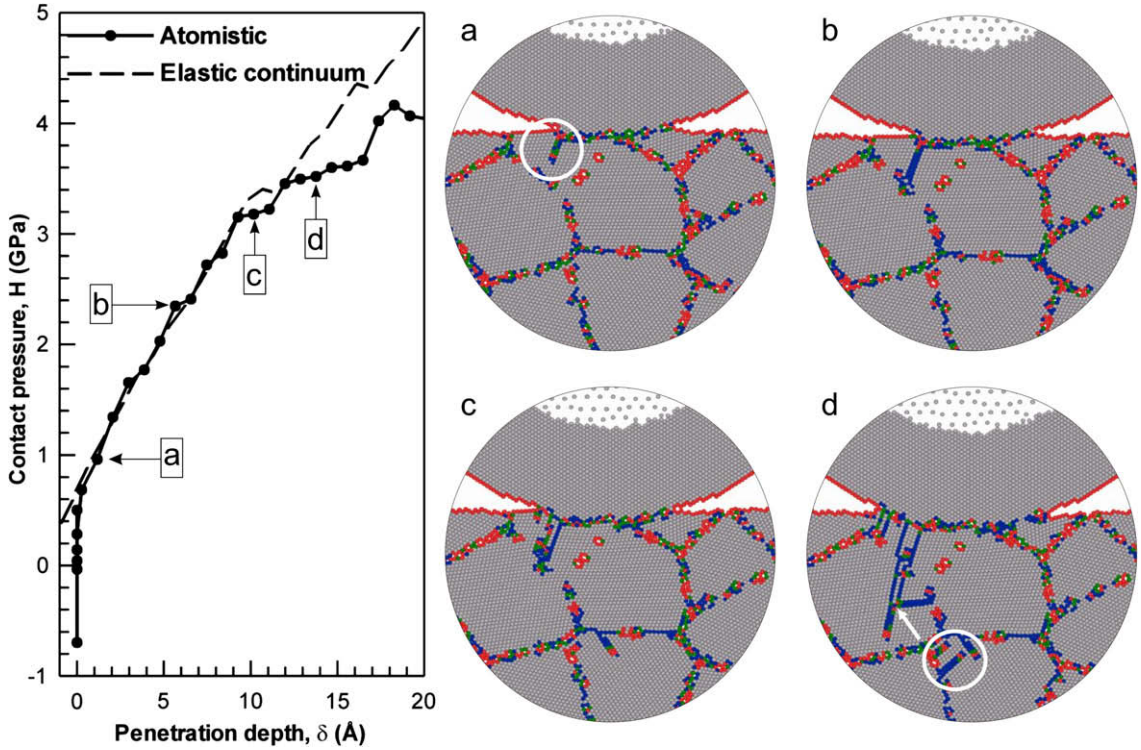

Fig. 7. Evolution of contact pressure as a function of penetration depth for shallow indentation using the Al-MF potential. Close-up views represent atomic details of deformation in the contact region. (a) Nucleation of the very first dislocation. (b) Elastic evolution of the structure. Nanocrystals (c) before and (d) after yielding point.

Table 2
Constitutive parameters extracted from force–displacement nanoindentation curves obtained by quasicontinuum simulation in nanocrystalline Al with a mean grain size of 7 nm

EAM potential	Contact pressure at yield point (GPa)	Contact pressure at depth δ_{max} (GPa)	δ_{max} (Å)	δ_f (Å)	δ_f/δ_{max} (%)
Al-VC	2.3	4.3	78.9	48.9	62
Al-MF	3.5	8.6	78.6	32.9	41

The parameters δ_f and δ_{max} represent the depth of the residual impression after unloading and the maximum penetration depth, respectively.

plastic flow serration is somewhat less intense with Al-VC than Al-MF. In the latter case, a clear change in slope occurs for a penetration depth of 34 Å, which corresponds to the propagation of an extensive shear band by intragranular slip through several grains (not shown here). Furthermore, it is shown in Figs. 6 and 7 that the contact pressures are almost identical between atomistic results and elastic theory until the two curves reach a depth of 10–15 Å. The divergence between elastic and atomistic curves marks the onset of plasticity from a macroscopic, continuum standpoint. These curves also provide direct evidence that the onset of plasticity occurs at significantly larger contact pressure in Al-MF potential than Al-VC potential. Table 2 summarizes several characteristics of the mechanical response as a function of the potential. The yield point was found to take place at a contact pressure of 2.3 GPa for the Al-VC potential and 3.5 GPa for the Al-MF potential. The pressure difference becomes more significant at the end of the indentation process, where contact pressures of 4.3 and 8.6 GPa are observed for the two potentials, respectively. Investigation of the depth of the residual impression after unloading also shows some significant differences in the constitutive response between the two potentials. In Table 2, the residual plastic depth δ_f is found equal to 48.9 and 32.9 Å for the Al-VC and Al-MF potentials, respectively, showing that the Al-VC model sustained 62% of plasticity, while the Al-MF model only 41%, for the same maximum depth of penetration.

3.4. Incipient mechanisms of plasticity at yield point ($\delta < 20$ Å)

Snapshots are included in Figs. 6 and 7 to show the deformation of the contact zone at four different loading steps. These steps correspond to the emission of the very first dislocation, and steps preceding or past the yield point shown in the pressure–displacement curves. In Fig. 6a, the Al-VC simulation is characterized by the emission of two dislocations from the contact interface, as circled, while the contact pressure is still negative because the tip has not yet indented the surface. During the elastic portion of the nanoindentation curve, a full dislocation from the tip–film interface, and two partial dislocations from a GB are emitted (Fig. 6b). The curve presents a sudden drop in contact pressure, just before the yield point, which can be explained by the increase in contact area as seen on the left side of the tip in Fig. 6c. The yield point occurs just after the drop in contact pressure. Fig. 6d shows that further emissions of partial dislocation occur, some of them interacting with one another as shown by the arrows on the left side of the tip. At the same time, a GB is observed

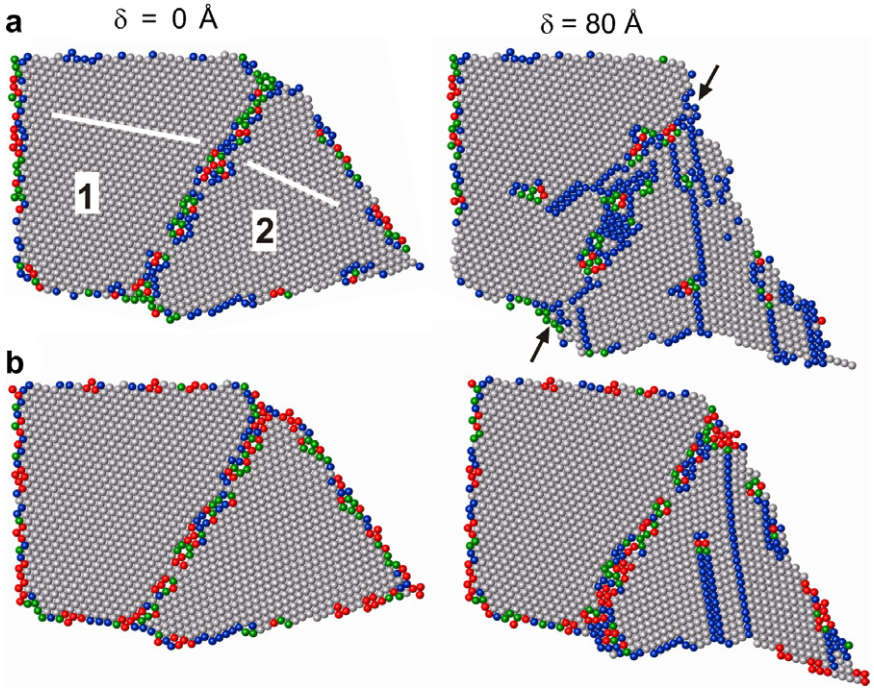

Fig. 8. Effects of interatomic potential on the structure of a low-angle GB ($\psi + \psi' \sim 164°$) before indentation ($\delta = 0$ Å) and at final indentation ($\delta = 80$ Å). (a) Al-VC potential; (b) Al-MF potential. Continuous lines indicate the [1 1 0] crystal lattice direction.

to migrate in order to align itself with a stacking fault present in a neighboring grain on the right side of the tip.

In Fig. 7a, for the Al-MF simulation, one partial dislocation is emitted before the yield point from the contact interface when a positive contact pressure is applied. No further dislocation activity, however, is observed during the elastic portion of the nanoindentation curve (Fig. 7b). At the yield point shown in Fig. 7c, a deformation twin is formed from the contact interface on the left side of the tip. After yielding, the deformation is more predominantly characterized by extensive dislocation activity emanating from GBs located one grain below the tip as circled in Fig. 7d. As in the Al-VC simulation, several partial dislocations, which are highlighted by arrows, intersect one another. No GB migration is observed in this case as opposed to the Al-VC simulation.

3.5. GB-mediated plasticity mechanisms ($\delta > 20$ Å)

In this section, attention is paid to the deformation mechanisms at larger penetration depths ($\delta > 20$ Å). As shown in Fig. 5, the contact response is distinguished by some significant plastic flow serration. This effect is found to be associated with highly localized shear zones resulting from one of three possible mechanisms: (1) the emission of partial dislocations and twins emanating from GBs and the contact interface, as well as their propagation and intersection through intragranular slip, (2) GB sliding and grain rotation and (3) stress-assisted GB migration coupled to shear deformation. Fig. 8 illustrates the atomic structure of a low-angle GB separating grains 1 and 2 ($\psi + \psi' = 164.5°$) before and after deformation at maximum indentation depth. There are only slight variations in GB structure after relaxation ($\delta = 0$ Å) between the two potentials. After deformation ($\delta = 80$ Å), marked differences exist at the boundary between grains 1 and 2. In particular, significant GB sliding takes place in the case of the Al-VC potential (Fig. 8a), whereas the grains show no relative movement with the Al-MF potential (Fig. 8b). The GB sliding event occurring in the former case results in a radical transformation of the GB structure, and the propagation of partial dislocations emitted from the boundary. We also observe in this case that the GB becomes the source for several full dislocations gliding into grain 1, while no lattice dislocation is emitted in this grain with the Al-MF potential (Fig. 8b).

A high-angle GB separating grains 3 and 4 ($\psi + \psi' = 117°$) is shown in Fig. 9 after relaxation and at mid-penetration ($\delta = 40$ Å). For this boundary, the plastic deformation is mostly governed by the propagation of partial dislocations nucleated from this boundary regardless of the potential used. Several partial dislocations are also emitted on adjacent {1 1 1} planes to form several deformation twins in grain 4. More dislocation emissions from the GB are visible in this grain with the Al-VC potential (Fig. 9a). With the Al-MF potential, however, some cross-slip interaction between an existing twin and a newly formed partial dislocation is present at the center of this

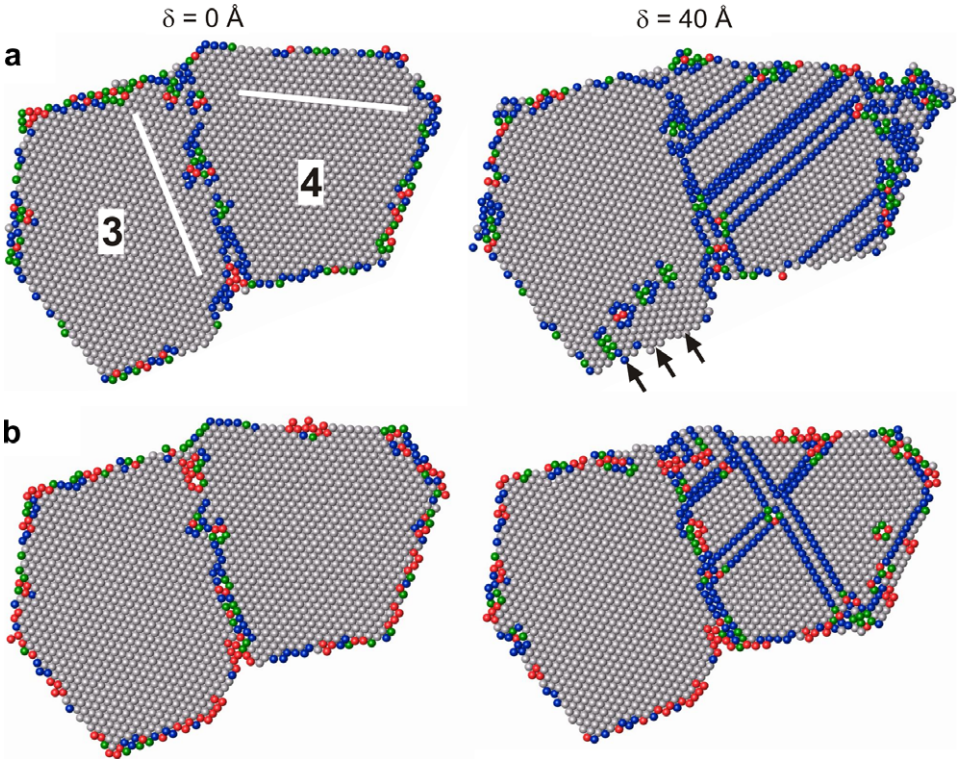

Fig. 9. Effects of interatomic potential on the structure of a high-angle GB ($\psi + \psi' \sim 117°$) before indentation ($\delta = 0$ Å) and at mid indentation ($\delta = 40$ Å). (a) Al-VC potential; (b) Al-MF potential. Continuous lines indicate the [1 1 0] crystal lattice direction.

grain (Fig. 9b), while no such interaction takes place with the Al-VC potential.

It can also be noticed in Fig. 9a for $\delta = 40$ Å that some GB motion occurs in the lower part of grain 3 for the Al-VC simulation. Fig. 10 represents this interface, which corresponds to a high-angle GB ($\psi + \psi' = 160.7°$) separating grains 3 and 5, although it is close to the limit between low- and high-angle GBs. This figure shows that GB migration is only observed for the Al-VC simulation. The original position of the GB before indentation is indicated by a dashed line for reference. The GB in the Al-VC simulation has moved about 34 Å into grain 3, whereas no significant differences are found with the Al-MF simulation, other than some minor rearrangements of GB atoms. In this GB migration process, it is clearly evident that the size of grain 3 has decreased while grain 5 has grown, which suggests that the mechanism is not associated with grain coalescence, but shear-coupled GB motion [41,82–87]. To support this hypothesis, we represent in Fig. 11 the evolution of the misorientation angle between grains 3 and 5. In this figure, the loading steps corresponding to the motion of the GB are represented by open circles. The two simulations present a small difference in misorientation angle of 1.3° after relaxation. Fig. 11 shows that the angle between the two grains remains almost constant during the entire simulation for the Al-MF potential. The average angle is

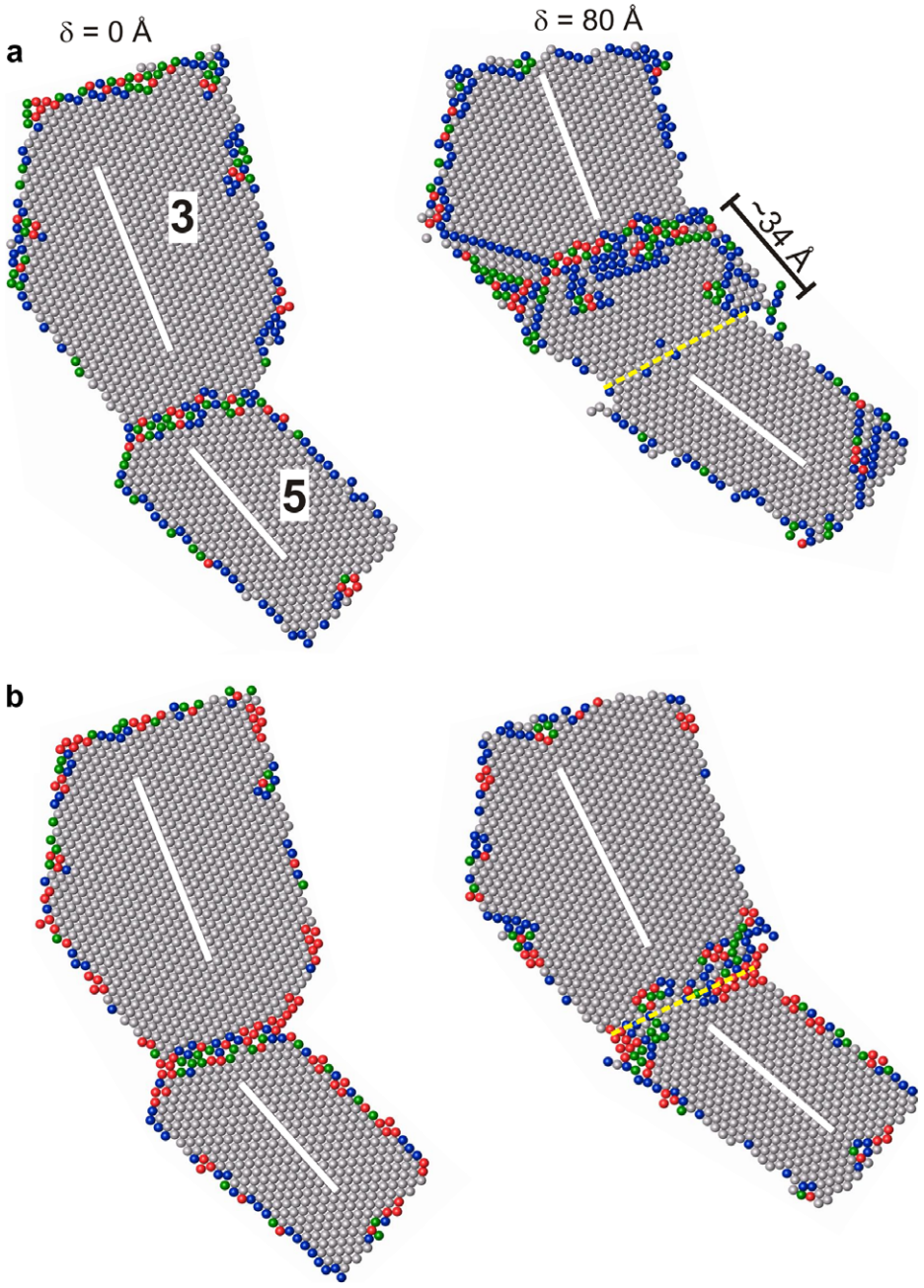

Fig. 10. Evolution of the GB structure at the interface between grains 3 and 5 for (a) Al-VC potential and (b) Al-MF.

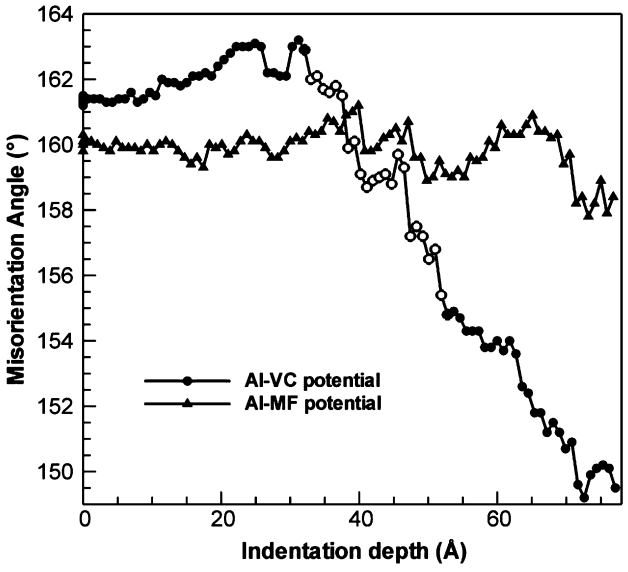

Fig. 11. Evolution of the misorientation angle at the interface between grains 3 and 5. Open symbols are used when the GB migrates, while plain symbols indicate that the GB is not moving.

found equal to 159.9° with a standard deviation of 0.62° in this case. The simulation performed with the Al-VC potential exhibits a totally different behavior, where the misorientation angle starts to increase from 161.4° to 163.2°, but then decreases. When the angle reaches 162°, GB migration is triggered. After the angle has dropped to 155.4°, GB migration is stopped, but the misorientation angle between the two grains keeps decreasing. These observations show evidence that the grain growth process is not due to grain rotation and coalescence; otherwise, the misorientation angle should have normally kept increasing until no particular misorientation prevails (i.e. $\psi + \psi' \sim 180°$).

4. Discussion

4.1. Similarities between simulation and experiments in nanocrystalline metal indentation

All experimental evidence for very small grain sizes (<20 nm) shows that the plastic deformation produced by nanosized contact tips involves inhomogeneous plastic deformation in highly localized shear zones [7,9,13,14]. The simulated contact response presented in Fig. 5 confirms this phenomenon, because plastic flow serration resulting from shear localization processes is observed with both potentials. The origin of the shear localization in this work is related to three atomic mechanisms, which are all mediated by GB deformation, as observed under uniaxial deformation [23–41,88]. These are: (1) the emission of partial dislocations and twins emanating from the contact interface and GBs, along with their propagation and intersection through intragranular slip, (2) GB sliding and grain rotation, and (3) stress-driven GB migration coupled to shear deformation. The occurrence of deformation twinning and stress-driven grain growth in nanocrystalline Al are in good agreement with past indentation studies [42,89]. Since our computer simulations are conducted in the athermal limit, no rate-limiting deformation mechanisms can be distinguished here. Nevertheless, this study allows us to conclude that small variations in stacking fault energy and GB energy, as predicted by the interatomic potential, can dramatically influence the modes of plastic deformation at GBs and hardness in nanocrystalline Al. More generally, this conclusion may somewhat reconcile the discrepancies found in earlier nanoindentation experiments about the incipient plasticity mechanisms for very small grain sizes in the nanocrystalline regime [10,42–46].

Furthermore, several commonalities exist between our simulation results and the in situ nanoindentation experiment of Minor et al. [12]. Both studies show that dislocation activity can occur at the very beginning of the indentation, before the "macroscopic" yield point deduced from load–displacement curves. Relating the atomic mechanisms of plasticity to the mechanical response using atomistic simulation further suggests that macroscopic yielding phenomena are caused by GB-mediated plastic processes in the film, such as partial dislocation emission from GBs (Fig. 7d) or GB migration (Fig. 6d), rather than by the propagation of dislocations emitted from the tip–film contact interface (Figs. 6a,b and 7a,b). This finding supports the idea that the yield point as measured by nanoscale contact probes is representative of local plasticity phenomena at GBs in nanocrystalline metal films with very small grain sizes, despite the creation of dislocations caused by deformation of the contact interface.

4.2. Effects of interatomic potential on GB-mediated plasticity and stress-driven grain growth

The salient feature of our simulations is the major difference in mechanical response and deformation mechanisms observed when we vary the interatomic potential. First, we find a pronounced strengthening effect in the overall contact pressure curve presented in Fig. 5 for the Al-MF potential, as opposed to the Al-VC potential. This effect is accompanied by a notable increase in mean contact pressure at yield, as shown in Section 3.3. The difference in mechanical response as a function of the potential can be largely explained by the occurrence of GB sliding and GB migration which are mostly found in the Al material promoting the lowest predicted stacking and GB energy values. We discuss below how impurities such as hydrogen can enhance such difference. In contrast, the simulation obtained with the Al-MF potential shows that plasticity is only dominated by the emission of partial dislocations, their propagation across crystals, and their interaction. An example of dislocation interaction causing cross-slip at the intersection between a partial dislocation and a twin boundary can be found in the center of grain 4 in Fig. 9b.

Such cross-slip may also contribute to strengthen the microstructure during indentation.

Furthermore, it appears from Table 1 that all the ratios γ_{SF}/γ_{USF} and $\gamma_{UTF}/\gamma_{USF}$ are similar, suggesting the same slip and twinning behavior regardless of the potential. But it is worth noting that the slip activity was found less intense and more localized with the Al-MF potential than the Al-VC potential. While the microstructures of our films are similar, we interpret this variation by the difference in mechanical behavior at GBs resulting from local changes in GB structure and energy as obtained from the two potentials in Fig. 4.

An essential result of this study is that the grain growth event shown in Fig. 10 only took place in the Al-VC simulation. Several factors (diffusion, stress, random walk, etc.) can account for grain growth in polycrystalline metals, but only stress-driven grain growth is possible in the present simulations. Also, it is acknowledged that stress-driven grain growth can be accomplished via two mechanisms: rotation-induced grain coalescence [28–35] or coupling of GB motion to shear deformation [35–41,82–87]. In the former case, a large amount of grain rotation caused by GB sliding and disclinations [90] must operate in order to cancel the crystal misorientation between neighboring grains. For example, this mechanism has been observed in the TEM study of Gai et al. [44] in nanocrystalline Cu deformed by a micro-hardness indenter. In the present study, however, the evolution of the misorientation angles represented in Fig. 11 shows clear evidence that the mechanism is not associated with grain coalescence, but shear-coupled GB motion, since the degree of misorientation actually increases at the interface between the two grains. In summary, we can conclude that the plastic flow is enhanced in the case of the Al-VC simulation because of the increased GB deformation activity in the form of GB sliding and coupled GB motion.

4.3. Incidence of impurity on flow stress and GB-mediated plasticity in nanocrystalline metals

To better interpret the effects of the potential in the plastic flow and underlying deformation mechanisms, it is clearly important to recall that the energy values calculated for stacking faults, twin faults and GBs as shown in Table 1 are significantly smaller for the Al-VC potential than the Al-MF potential. One main source of discrepancy between different EAM potentials is related to the calibration of the density function. In the Al-MF potential, the electron density function is fitted based on ab initio and experimental values for surface and planar fault energies in high-purity Al [64]. On the contrary, the Al-VC potential empirically uses an electron density function of a 4s hydrogenic orbital, which, as stated by Voter and Chen [63], was chosen for describing first row transition metals, but was also found to work well for a number of fcc metals. This approximation may cause some significant change in cohesive energy during slip, as well as, local GB energy, as found in Fig. 4. Qualitatively, we find in Table 1 that the stacking fault energies and GB energy in Al crystals with impurities would be better modeled with the Al-VC potential than the Al-MF potential. The most common impurities in nanocrystalline Al are H, C, O and N impurities [36,39,91]. Impurities such as H atoms can either decrease the Peierls stress for slip and enhanced local plasticity in Al [92,93] or increase embrittlement at GBs [94–96]. Larger impurities present at grain boundaries can also prevent GB motion and stabilize the grain size [97–100]. Unfortunately, the treatment of impurities at GBs in FCC metals via proper formalisms, such as local chemical potential [101], is beyond the scope of the present study. However, this study emphasizes the crucial role of non-equilibrium GBs [102] and their local atomic structure in governing incipient plasticity in nanocrystalline metals.

5. Conclusions

We have examined the contact behavior and plasticity of a model nanocrystalline fcc metal with a mean grain size of 7 nm using multiscale simulations. The major conclusions of this work can be summarized as follows:

1. Macroscopic yielding phenomena are caused by GB-mediated plastic processes rather than by the propagation of dislocations emitted from the tip–film contact interface. The yield point as measured by nanoscale contact probes is representative of macroscopic yielding phenomena.
2. The contact pressure–displacement curves are found to display significant flow serration. This effect is associated with highly localized shear deformation resulting from one of three possible mechanisms: (1) the nucleation, propagation and interaction of partial dislocations and twins emanating from the contact interface and GBs, (2) GB sliding and grain rotation, and (3) stress-driven GB migration.
3. Significant differences in mechanical behavior exist between the interatomic potentials used. The propensity to localize the plastic deformation at GBs via interface sliding and coupled GB migration is greater in the Al material presenting the lowest predicted stacking fault energy and GB energy.
4. The mechanism of stress-driven grain growth was found associated with shear-coupled GB motion, rather than rotation-induced grain coalescence. Coupled GB motion was found to occur only in the simulation with the lowest predicted stacking fault energy and GB energy. This finding could therefore suggest a new means to control stress-assisted grain growth mechanisms by altering the local structure and energies at GBs, as suggested earlier in nanocrystalline metals under uniaxial deformation.

Acknowledgements

Support from the National Science Foundation CAREER program (Grant DMR-0747658) is gratefully acknowledged. The simulations presented in this work were performed using the quasicontinuum code by Tadmor and Miller [103].

References

[1] Nieman GW, Weertman JR, Siegel RW. Scripta Metal 1989;23:2013.
[2] Elsherik AM, Erb U, Palumbo G, Aust KT. Scripta Metal Mater 1992;27:1185.
[3] Fougere GE, Weertman JR, Siegel RW. NanoStruct Mater 1995;5:127.
[4] Qin XY, Wu XJ, Zhang LD. NanoStruct Mater 1995;5:101.
[5] Farhat ZN, Ding Y, Northwood DO, Alpas AT. Mater Sci Eng A 1996;206:302.
[6] Sanders PG, Eastman JA, Weertman JR. Acta Mater 1997;45:4019.
[7] Malow TR, Koch CC, Miraglia PQ, Murthy KL. Mater Sci Eng A 1998;252:36.
[8] Schiøtz J, Jacobsen KW. Science 2003;301:1357.
[9] Trelewicz JR, Schuh CA. Acta Mater 2007;55:5948.
[10] Chang SY, Chang TK. J Appl Phys 2007;101:033507.
[11] Yang B, Vehoff H. Acta Mater 2007;55:849.
[12] Minor AM, Syed Asif SA, Shan Z, Stach EA, Cyrankowski E, Wyrobek TJ, et al. Nat Mater 2006;5:697.
[13] Andrievski RA, Kalinnikov GV. J Mater Sci 2000;35:2799.
[14] Van Vliet KJ, Tsikata S, Suresh S. Appl Phys Lett 2003;83:1441.
[15] Kim JJ, Choi Y, Suresh S, Argon AS. Science 2002;295:654.
[16] Jana S, Bhowmick R, Kawamura Y, Chattopadhyay K, Ramamurty U. Intermetallics 2004;12:1097.
[17] Shi Y, Falk ML. Appl Phys Lett 2005;86:011914.
[18] Su C, Anand L. Acta Mater 2006;54:179.
[19] Castellero A, Lloyd SJ, Madge SV, Kovacs ZS, Löffler JF, Baricco M, et al. J Alloys Compd 2007;434–435:48.
[20] Antoniou A, Bastawros A, Biner B. J Mater Res 2007;22:514.
[21] Lund AC, Schuh CA. Mater Res Soc Symp Proc 2004;806. MM7.4.1-MM7.4.6.
[22] Sansoz F, Dupont V. Mater Sci Eng C 2007;27:1509.
[23] Yamakov V, Wolf D, Phillpot SR, Mukherjee AK, Gleiter H. Nat Mater 2002;1:45.
[24] Van Swygenhoven H, Derlet PM, Hasnaoui A. Phys Rev B 2002;66:024101.
[25] Tschopp MA, McDowell DL. Scripta Mater 2008;58:299.
[26] Schiøtz J, Di Tolla FD, Jacobsen KW. Nature 1998;391:561.
[27] Schiøtz J, Vegge T, Di Tolla FD, Jacobsen KW. Phys Rev B 1999;60:11971.
[28] Hasnaoui A, Van Swygenhoven H, Derlet PM. Phys Rev B 2002;66:184112.
[29] Wei Q, Jia D, Ramesh KT, Ma E. Appl Phys Lett 2002;81:1240.
[30] Shimokawa T, Kinari T, Shintaku S, Nakatani A. Model Simul Mater Sci Eng 2006;14:S63.
[31] Fan GJ, Wang YD, Fu LF, Choo H, Liaw PK, Ren Y, Browning ND. Appl Phys Lett 2006;88:171914.
[32] Joshi SP, Ramesh KT. Acta Mater 2008;56:282.
[33] Wang YB, Li BQ, Sui ML, Mao SX. Appl Phys Lett 2008;92:011903.
[34] Yang B, Vehoff H, Hohenwarter A, Hafok M, Pippan R. Scripta Mater 2008;58:790.
[35] Haslam AJ, Phillpot SR, Wolf D, Moldovan D, Gleiter H. Mater Sci Eng A 2001;318:293.
[36] Gianola DS, Van Petegem S, Legros M, Brandstetter S, Van Swygenhoven H, Hemker KJ. Acta Mater 2006;54:2253.
[37] Farkas D, Frøseth A, Van Swygenhoven H. Scripta Mater 2006;55:695.
[38] Gianola DS, Warner DH, Molinari JF, Hemker KJ. Scripta Mater 2006;55:649.
[39] Gianola DS, Mendis BG, Ceng XM, Hemker KJ. Mater Sci Eng A 2008;483–484:637.
[40] Gianola DS, Eberl C, Cheng X, Hemker KJ. Adv Mater 2008;20:303.
[41] Gutkin MY, Mikaelyan KN, Ovid'ko IA. Scripta Mater 2008;58:850.
[42] Jin M, Minor AM, Stach EA, Morris Jr JW. Acta Mater 2004;52:5381.
[43] Zhang K, Weertman JR, Eastman JA. Appl Phys Lett 2005;87:061921.
[44] Gai PL, Zhang K, Weertman J. Scripta Mater 2007;56:25.
[45] Chen J, Wang W, Qian LH, Lu K. Scripta Mater 2003;49:645.
[46] Li H, Ngan AHW. Mater Res Soc Symp Proc 2005;841:R8.7.1.
[47] Feichtinger D, Derlet PM, Van Swygenhoven H. Phys Rev B 2003;67:024113.
[48] Lilleodden ET, Zimmerman JA, Foiles SM, Nix WD. J Mech Phys Sol 2003;51:901.
[49] Ma XL, Yang W. Nanotechnology 2003;14:1208.
[50] Jang H, Farkas D. Mat Res Soc Symp Proc 2004;821:P8.17.1.
[51] Hasnaoui A, Derlet PM, Van Swygenhoven. Acta Mater 2004;52:2251.
[52] Saraev D, Miller RE. Model Simul Mater Sci Eng 2005;13:1089.
[53] Kim KJ, Yoon JH, Cho MH, Jang H. Mater Lett 2006;60:3367.
[54] Jang H, Farkas D. Mater Lett 2007;61:868.
[55] Dupont V, Sansoz F. Mater Res Soc Symp Proc 2006;903E:0903-Z06-051-0903-Z06-05.6.
[56] Sansoz F, Dupont V. In: Proceedings of the NSTI nanotech 2006 conference 2006;1:50.
[57] Sansoz F, Dupont V. Appl Phys Lett 2006;89:111901.
[58] Szlufarska I, Nakano A, Vashishta P. Science 2005;309:911.
[59] Zimmerman JA, Gao H, Abraham FF. Model Simul Mater Sci Eng 2000;8:103.
[60] Miller RE, Tadmor EB. J Comput Aided Mater Des 2002;9:203.
[61] Voronoi GZ. J Reine Angew Math 1908;134:199.
[62] Kelchner CL, Plimpton SJ, Hamilton JC. Phys Rev B 1998;58:11085.
[63] Voter AF, Chen SP. Mat Res Soc Symp Proc 1987;82:175.
[64] Mishin Y, Farkas D, Mechl MJ, Papaconstantopoulos DA. Phys Rev B 1999;59:3393.
[65] Sansoz F, Molinari JF. Scripta Mater 2004;50:1283.
[66] Sansoz F, Molinari JF. Acta Mater 2005;53:1931.
[67] Johnson KL. Contact mechanics. Cambridge: Cambridge University Press; 2003.
[68] Meyers MA, Chawla KK. Mechanical behavior of materials. Upper Saddle River, NJ: Prentice Hall; 1999.
[69] Van Swygenhoven H, Derlet PM, Frøseth AG. Nat Mater 2004;3:399.
[70] Murr LE. Interfacial phenomena in metals and alloys. Reading, MA: Addison-Wesley; 1975.
[71] Rautioaho RH. Phys Status Solid B 1982;112:83.
[72] Westmacott KH, Peck RL. Philos Mag 1971;23:611.
[73] Ogata S, Li J, Yip S. Science 2002;298:807.
[74] Hartford J, von Sydow B, Wahnström G, Lundqvist BI. Phys Rev B 1998;58:2487.
[75] Lu G, Kioussis N, Bulatov VV, Kaxiras E. Phys Rev B 2000;62:3099.
[76] Bernstein N, Tadmor EB. Phys Rev B 2004;69:094116.
[77] Lu G, Orlikowski D, Park I, Politano O, Kaxiras E. Phys Rev B 2002;65:064102.
[78] Qi Y, Mishra RK. Phys Rev B 2007;75:224105.
[79] Inoue Y, Uesugi T, Takigawa Y, Higashi K. Mater Sci Forum 2007;561–656:1837.
[80] Wright AF, Atlas SR. Phys Rev B 1994;50:15248.

[81] Thomson DI, Heine V, Payne MC, Marzari N, Finnis MW. Acta Mater 2000;48:3623.
[82] Cahn JW, Taylor JE. Acta Mater 2004;52:4887.
[83] Cahn JW, Mishin Y, Suzuki A. Acta Mater 2006;54:4953.
[84] Gutkin MY, Ovid'ko IA. Appl Phys Lett 2005;87:251916.
[85] Molodov DA, Ivanov VA, Gottstein G. Acta Mater 2007;55:1843.
[86] Ovid'ko IA, Sheinerman AG, Aifantis EC. Acta Mater 2008;56:2718.
[87] Li JCM. Phys Rev Lett 2006;96:215506.
[88] Farkas D, Mohanty S, Monk J. Mater Sci Eng A, 2008;493:33.
[89] Chen M, Ma E, Hemker K, Sheng H, Wang Y, Cheng X. Science 2003;300:1275.
[90] Ovid'ko IA, Sheinerman AG. Scripta Mater 2008;59:119.
[91] Rajagopalan J, Han JH, Saif MTA. Science 2007;315:1831.
[92] Myers SM, Baskes MI, Birnbaum HK, Corbett JW, DeLeo GG, Estreicher SK, et al. Rev Modern Phys 1992;64:559.
[93] Lu G, Zhang Q, Kioussis N, Kaxiras E. Phys Rev Lett 2001;87:095501.
[94] Geng WT, Freeman AJ, Wu R, Geller CB, Raynolds JE. Phys Rev B 1999;60:7149.
[95] Liu X, Wang X, Wang J, Zhang H. J Phys Condens Matter 2005;17:4301.
[96] Lu G, Kaxiras E. Phys Rev Lett 2005;94:155501.
[97] Millet PC, Selvam RP, Bansal S, Saxena A. Acta Mater 2005;53:3671.
[98] Millet PC, Selvam RP, Saxena A. Acta Mater 2006;54:297.
[99] Millet PC, Selvam RP, Saxena A. Mater Sci Eng A 2006;431:92.
[100] Millet PC, Selvam RP, Saxena A. Acta Mater 2007;55:2329.
[101] Elsener A, Politano O, Derlet PM, Van Swygenhoven H. Model Simul Mater Sci Eng 2008;16:025006.
[102] Hasnaoui A, Van Swygenhoven H, Derlet PM. Acta Mater 2002;50:3927.
[103] Tadmor EB, Miller RE. The QC method homepage. Available from: http://www.qcmethod.com.